PHYSICAL REVIEW RESEARCH **6**, 023045 (2024)

**Editors' Suggestion**

# Modulation instability and wavenumber bandgap breathers in a time layered phononic lattice

Christopher Chong,[1] Brian Kim,[2] Evelyn Wallace,[1] and Chiara Daraio[2]
[1]*Department of Mathematics, Bowdoin College, Brunswick, Maine 04011, USA*
[2]*Department of Mechanical and Civil Engineering, California Institute of Technology, Pasadena, California 91125, USA*

(Received 11 October 2023; accepted 11 March 2024; published 11 April 2024)

We provide the first experimental realization of wavenumber bandgap ($q$-gap) breathers. Experiments are obtained in the setting of a time-periodic phononic lattice where the model and experiment exhibit good qualitative agreement. $q$-gap breathers are localized in time and periodic in space, and are the counterparts to the classical breathers found in space-periodic systems. We derive an exact condition for modulation instability that leads to the opening of wavenumber bandgaps in which the $q$-gap breathers can arise. The $q$-gap breathers become more narrow and larger in amplitude as the wavenumber goes further into the bandgap. In the presence of damping, these structures acquire a nonzero, oscillating tail. The controllable temporal localization that $q$-gap breathers make possible has potential applications in the creation of phononic frequency combs, energy harvesting or acoustic signal processing.

DOI: 10.1103/PhysRevResearch.6.023045

## I. INTRODUCTION

The classical discrete breather is a spatially localized, time-periodic structure found in areas as diverse as photonics, electrical circuits, condensed-matter physics, molecular biology, chemistry, and phononics [1]. Breather spatial localization has been exploited for the purpose of information storage and transfer in the context of photonic crystals [2] and proposed for energy harvesting applications in phononic lattices embedded with piezoelectric sensors [3]. Breathers also find use in modeling the pairing and unpairing of the DNA double strand [4], and in the targeted breaking of chemical bonds [5]. These are just some of the applications that were motivated by the discovery of breathers as an alternate mechanism for localization. Comprehensive reviews such as [1,6,7] summarize the rich history of discrete breathers. A key defining feature of the discrete breather is that its temporal frequency lies within a frequency gap [1]. Spatially periodic media can have frequency gaps, and hence, discrete breathers are possible in such systems, see Fig. 1(a) for an illustration.

Other types of localization have been studied since the discovery of discrete breathers, including localization in wavenumber (whose corresponding solutions have been coined $q$-breathers) [8], and temporal localization via mechanisms such as zero-wavenumber gain modulation instability [9] and nonlinear resonances [10,11]. The so-called Akhmediev breathers of the nonlinear Schrödinger (NLS) equation [12], and its discrete integrable counter-part, the Ablowtiz-Ladik lattice [13], are also localized in time. The Peregrine soliton of the NLS equation is localized in both space and time. Peregrine solitons have been proposed in explaining the formation of so-called rogue waves found in the ocean, atmosphere and in a host of other settings [14]. The existence of Akhmediev breathers and Peregrine solitons relies on the integrability of the underlying equations, and hence are quite special. While the structures just listed also feature localization, arguably, the most natural counterpart to the classical discrete breather is the so-called wavenumber bandgap ($q$-gap) breather. It has the same defining features of the classic breather, but the role of space and time are switched. In particular, a $q$-gap breather is localized in time, periodic in space and, importantly, has a wavenumber that lies in a $q$-gap, see Fig. 1(b). This latter feature distinguishes $q$-gap breathers from other temporally localized structures and better completes the analogy to the classical discrete breather. Moreover, it specifies a robust mechanism for the formation of $q$-gap breathers, namely, the opening of a $q$-gap. Wavenumber bandgaps can be found in a wide class of temporally periodic lattices (also called time-crystals). Indeed, there have been many recent advances in experimental platforms for time-varying systems, including photonic [15–18], electric [19–21], and phononic examples [22–34]. Despite the availability of time-varying platforms and the natural connection to the classical breather, $q$-gap breathers have received little attention in the literature. Indeed, the existence of such solutions was first established theoretically in a photonic time crystal (PTC) only very recently [35] (where they were called $k$-gap solitons). While [35] proposes an experimental approach for the detection of such solutions, there are currently no reports on their experimental realization. $q$-gap breathers represent a new class of solutions and are the focus of the present paper. We detail how they can be robustly generated and provide the first experimental realization of $q$-gap breathers found in any system. This is done in the context of a phononic lattice. Controllable temporal localization has potential applications in the creation of phononic

---

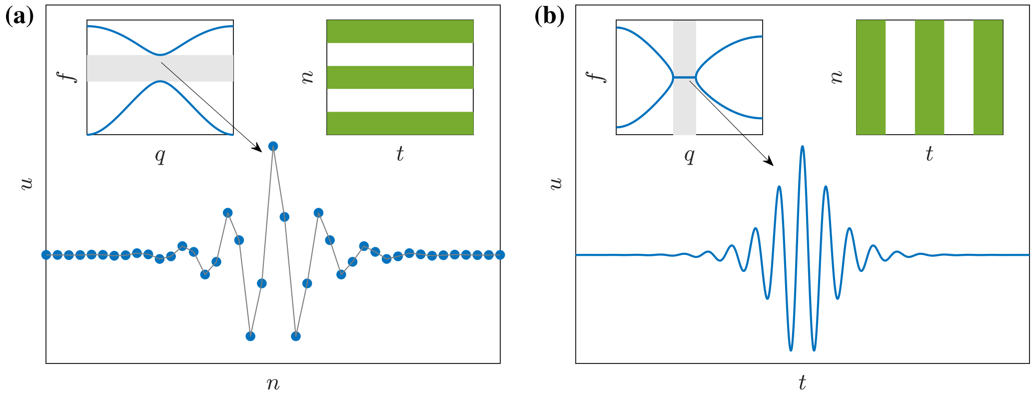

FIG. 1. (a) Illustration of a classical discrete breather, which is localized in space and periodic in time. The linear spectrum is shown in the left inset, where the frequency $f$ is plotted against the wavenumber $q$. The spectrum has a frequency gap, which is induced by the spatial periodicity of the medium. A schematic of the underlying medium is shown in the right inset. The frequency of the breather lies in the frequency gap (horizontal gray shaded region in the spectrum shown in the left inset). (b) Illustration of a wavenumber bandgap ($q$-gap) breather (the focus of the present paper), which is localized in time and periodic in space. The linear spectrum is shown in the left inset, where the frequency $f$ is plotted against the wavenumber $q$. The spectrum has a wavenumber gap, which is induced by the temporal periodicity of the medium (right inset). The wavenumber of the breather lies in the $q$-gap (vertical gray shaded region in the spectrum shown in the left inset).

frequency combs [10,11,36], energy harvesting [37,38], or acoustic signal processing [39]. The alternate mechanism for temporal localization that $q$-gap breathers afford and the wide availability of platforms in which they may be implemented suggest the potential utility of $q$-gap breathers in photonic, phononic, electrical, and even chemical or biological applications.

The paper is organized as follows: In Sec. II, we introduce the experimental platform and underlying model equations. In Sec. III, we derive an exact condition for the opening of wavenumber bandgaps and compare the analytical stability predictions against experimental results. Families of $q$-gap breathers that emerge from the wavenumber bandgaps are explored in Sec. IV numerically and experimentally. Conclusions and avenues of future work are discussed in Sec. V.

## II. EXPERIMENTAL AND MODEL SETUP

We start by describing a time-periodic medium that corresponds to the schematic in the right inset of Fig. 1(b). In particular, we consider a phononic lattice that consists of repelling magnetic masses with grounding stiffness controlled by electrical coils. The experimental setup is adapted from the platform developed in Refs. [24,34]. The chain is composed of $N-1$ ring magnets (K&J Magnetic, Inc., P/N R848) lined with sleeve bearings (McMaster-Carr P/N 6377K2) comprising the uniform masses, arranged with alternating polarity on a smooth rod (McMaster-Carr P/N 8543K28). Electromagnetic coils (APW Company SKU: FC-6489) are fixed concentrically around the equilibrium positions of each of the innermost eight masses, such that they may exert a restoring force on each mass proportional to the current induced by applied voltage step-function (Aglient 33220A, Accel Instruments TS250-2). The velocity of each mass is measured using laser Doppler vibrometer (Polytec CLV-2534), repeating experiments to a construct full velocity field for the lattice. Figure 2 shows a schematic of the experimental setup.

The system is modeled as Fermi-Pasta-Ulam-Tsingou–type (FPUT-type) lattice [24,34,40]

$$M\ddot{u}_n + k(t)\,u_n + c\dot{u}_n = F(u_n - u_{n-1}) - F(u_{n+1} - u_n), \quad (1)$$

where $u_n$ is the displacement of the $n$th ring magnet from its equilibrium position, where the equilibrium distance between adjacent magnets is $d = 0.0334$ m. The indices run from $n = 1, \dots, N-1$ and we consider fixed boundary conditions $u_0(t) = u_N(t) = 0$. All ring magnets have uniform mass $M = 0.0097$ kg. Dissipative forces are modeled with a phenomenological viscous damping term $c du_n/dt$, where the damping coefficient $c = 0.15$ N s/m is determined empirically by matching the simulated and experimental spatial decay of the velocity amplitude envelope of waves traveling through the lattice [34]. The experimentally measured force-distance relation between neighboring masses is fit with a dipole-dipole approximation, as in Ref. [24], which is given by $F(x) = A(d+x)^{-\alpha}$, where $x$ is the center-to-center distance between masses with $A = 9.044 \times 10^{-7}$ N m$^4$ and $\alpha = 4$. The current resulting from a periodic step function voltage applied to the electromagnetic coils induces a magnetic field

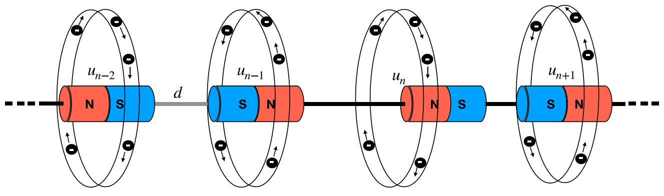

FIG. 2. Schematic of the modulated magnetic lattice. The masses with north (N) and south (S) magnetic poles are arranged to be repelling, which provides nonlinear intersite coupling. The rings surrounding the magnets are the electromagnetic coils that induce an onsite stiffness that can be controlled dynamically. This provides the possibility of a time-varying lattice. The equilibrium distance between adjacent magnets is $d$.

that provides a grounding stiffness modulation of the form

$$k(t)=\begin{cases}k_a, & 0\leqslant t<\tau T\\ k_b, & \tau T\leqslant t<T,\end{cases}\qquad k(t)=k(t+T). \tag{2}$$

The step values $k_a, k_b$ and duty-cycle $0<\tau<1$ are parameters. With this choice of stiffness, the medium is periodic in time but constant in space [see the right inset of Fig. 1(b)]. A medium of this type is a direct analogy of a spatially periodic lattice in which classical discrete breathers are possible, see the right inset of Fig. 1(a).

We use the modulation frequency $f_{\text{mod}}=1/T$ Hz as the main system parameter to be varied, but we also consider various values of $k_b$, $\tau$, and $c$. The parameters $M, d, A, \alpha$, and $k_a=0$ will be fixed throughout the paper. With the exception of one example in the Appendix, the lattice length parameter is fixed to $N=11$.

## III. MODULATION INSTABILITY

To find breathers, we first need to determine the wavenumber bandgap, an example of which is illustrated in the left inset of Fig. 1(b). This is achieved by computing the stability of plane waves (i.e., the modulation stability) of the linearized model

$$M\ddot{u}_n=K(u_{n-1}-2u_n+u_{n+1})-k(t)u_n-c\dot{u}_n, \tag{3}$$

where $K=\alpha Ad^{\alpha-1}$. The linearized equation is obtained by keeping the linear terms in the Taylor expansion of the nonlinear coupling force $A(d+y)^{-\alpha}$, where it is assumed that $|u_n-u_{n-1}|\ll d$ for $n=1,\dots,N-1$. For time-independent stiffness $[k(t)=0]$, the undamped $(c=0)$ linear equation has the dispersion relationship $\omega^2_{\text{disp}}(q)=4K/M\sin^2(q/2)$. In the case of time-dependent stiffness $[k(t)\neq 0]$, a gap in the wavenumber axis $q$ is possible [41]. For general time-periodic stiffness $k(t)$, a wavenumber bandgap will open where the dispersion curve $\omega_{\text{disp}}(q)$ intersects itself when translated by an integer multiple of half the modulation frequency [41]. In general, the modified dispersion relation must be computed numerically or approximated analytically. Example approximate approaches include a plane-wave expansion [41] or reduction of the equations of motion to a system where the dispersion relation can be computed explicitly, as in Ref. [35] (where coupled-mode equations are derived). In the case of sinusoidal modulation (leading to a Mathieu-type equation), the dispersion relation can be approximated using perturbation analysis [34,42]. The advantage of considering $k(t)$ to be a periodic step function is that the modified dispersion relation can be computed exactly, which we now demonstrate.

Making the ansatz $u_n(t)=X_m(n)\Theta_m(t)$, one finds upon substitution into Eq. (3) and enforcing Dirichlet boundary conditions that the eigenfunctions are $X_m(n)=\sin(q_m n)$ where the wavenumber is $q_m=m\pi/N$ with $m=1,\dots,N-1$. In the infinite lattice, $q\in[0,\pi]$. The associated eigenvalues are $\lambda_m=\sin^2(q_m/2)$. The temporal part $\Theta(t)$ satisfies

$$M\ddot{\Theta}_m=-[\lambda_m K+k(t)]\Theta_m-c\dot{\Theta}_m. \tag{4}$$

The general solution of Eq. (4) will be a superposition of functions of the form $\Theta_m(t)=H_m(t)e^{\mu_m t}$ where $H_m(t)$ has period $T$ and $\mu_m=\sigma_m+i\omega_m$ is the Floquet exponent where $\sigma_m,\omega_m\in\mathbb{R}$. The Floquet multiplier is $e^{\mu_m T}$. The waveform associated with the wavenumber $q_m$ will be stable if $\sigma_m\leqslant 0$, or equivalently, if the Floquet multiplier has modulus less than unity, $|e^{\mu_m T}|\leqslant 1$. The modified dispersion relationship is obtained by plotting the imaginary part of the Floquet exponent, $\omega$, against the wavenumber $q$ [see the blue lines of the inset of Fig. 1(b)]. Since growth is possible, it is also instructive to plot the real part of the Floquet exponent, $\sigma$, see Fig. 3(a).

In the case that the stiffness $k(t)$ is a periodic step function, see Eq. (2), $\Theta_m(t)$ can be computed explicitly by adapting a procedure carried out in the context of an undamped Kronig-Penney photonic lattice [43,44]. In particular, we make the ansatz

$$H_m(t)=\begin{cases}H_{a,m}(t), & 0\leqslant t<\tau T\\ H_{b,m}(t), & \tau T\leqslant t<T,\end{cases} \tag{5}$$

where $H_{a,m}(t)$ and $H_{b,m}(t)$ are the general solutions to Eq. (4) on the intervals $0\leqslant t<\tau T$ and $\tau T\leqslant t<T$, respectively. Such explicit general solutions are available since Eq. (4) is constant on these intervals. Demanding that $H_{a,m}(\tau T)=H_{b,m}(\tau T)$ and $\dot{H}_{a,m}(\tau T)=\dot{H}_{b,m}(\tau T)$ ensures continuity at the interface and demanding that $H_{a,m}(0)=H_{b,m}(T)$ and $\dot{H}_{a,m}(0)=\dot{H}_{b,m}(T)$ ensures that $H_m$ is $T$ periodic. These four equations have a determinant condition that can be expressed as (detailed in Appendix A)

$$G=\cosh\left[\left(\sigma_m+\frac{c}{2M}\right)T\right]\cos(\omega_m T), \tag{6}$$

$$0=\sinh\left[\left(\sigma_m+\frac{c}{2M}\right)T\right]\sin(\omega_m T), \tag{7}$$

where $G$ depends on the wavenumber and system parameters, but not the Floquet exponent $\mu_m$:

$$G\equiv-\frac{s(k_a)^2+s(k_b)^2}{2s(k_a)s(k_b)}\sin[s(k_a)\tau T]\sin[s(k_b)(1-\tau)T]$$
$$+\cos[s(k_a)\tau T]\cos[s(k_b)(1-\tau)T],$$

where $s(k)=[4M(\lambda_m K+k)-c^2]^{1/2}/(2M)$. These equations allow for the exact computation of the Floquet exponents $\mu_m=\sigma_m+i\omega_m$. An example plot is shown in Fig. 3(a). If $|G|\leqslant 1$ then $\sigma_m=-c/(2M)$ and $\omega_m=\cos^{-1}(G)/T$. In this case the underlying solution is stable. If $\pm G>1$ then $\omega_m=(3\pm 1)\pi/(2T)$, implying that the imaginary part of the Floquet exponent is an integer multiple of half the modulation frequency, which is consistent with situation in general time-periodic lattices [41]. In this case, the real part of the Floquet exponent is $\sigma_m=\pm\cosh^{-1}(\mp G)/T-c/(2M)$ which implies the following condition for stability,

$$|G_D|\leqslant 1,\qquad G_D\equiv G\,\text{sech}\left(\frac{cT}{2M}\right). \tag{8}$$

Note that this expression is exact and gives an efficient way to check for stability via direct substitution of the system parameters into $G_D$ and simply checking the inequality. A plot of $G_D$ is shown in Fig. 3(b). The set of wavenumbers where $|G_D|>1$ make up the so-called wavenumber bandgap. The edges can be found by solving $G_D=\pm 1$. See the gray regions of Fig. 3, and the inset of Fig. 1(a) for example wavenumber bandgaps.

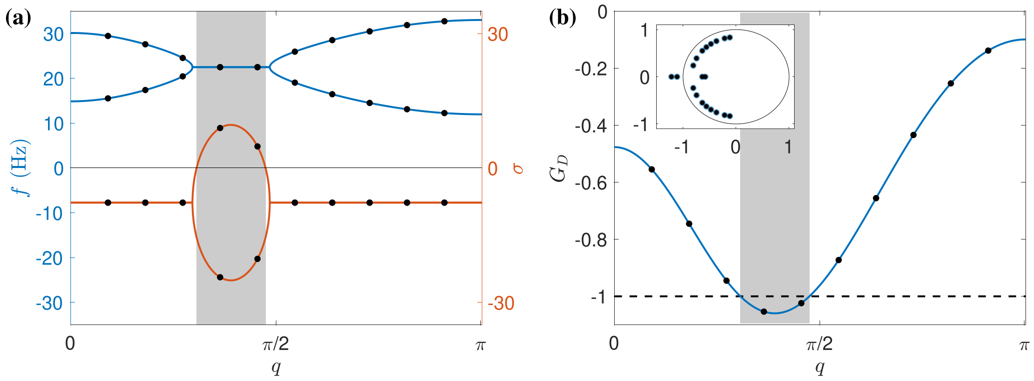

FIG. 3. (a) Plot of the modified dispersion relation for the time-varying lattice with $k_b = 150$ N/m, $\tau = 0.5$, $c = 0.15$ N s/m, and $f_{\mathrm{mod}} = 45$ Hz in the infinite lattice. In particular, $f = \omega/(2\pi)$ (blue curve) and $\sigma$ (red curve) are shown against the wavenumber $q$, where $\omega$ is the imaginary part of the Floquet exponent and $\sigma$ is the real part of the exponent. The black dots show the corresponding values for a finite sized lattice with $N = 11$. The shaded gray region indicates the region of instability (i.e., the wavenumber bandgap). (b) Plot of the function $G_D$ from Eq. (8) in the infinite lattice (solid blue line) and in the $N = 11$ lattice (black dots). The plane wave is unstable when $|G_D| > 1$, which is highlighted by the gray region. The inset shows the corresponding Floquet multipliers in the complex plane. There are two multipliers lying outside the unit circle (also shown) demonstrating the instability of a general solution.

The theoretical linear stability predictions can be compared with experimental observations. We fix all parameters other than the modulation frequency ($f_{\mathrm{mod}}$) and amplitude ($k_b$). In Fig. 4 we show the stability diagram for various values of the duty cycle $\tau$. Red indicates instability ($|G_D| > 1$) and blue indicates stability ($|G_D| \leqslant 1$). The white markers superimposed on the figure are the parameter values where the zero state in experiment was observed to be unstable. A solution is considered unstable in the experimental setup if an initially at rest lattice does not come to rest after being excited on one boundary by an impulse (a stroke of $\leqslant$0.015 m at approximately 0.4 m/s). If it does come to rest, it is classified as stable. There is good qualitative agreement between the model predictions and the experiments. Plausible sources of discrepancy between model and experiment include the linearization of the modulating coil force, possible nonlinearity of the frictional forces and the impedance of the system distorting the relatively high current signals for the modulation. Additionally, in the experiment, modulation is not applied to the first and last nodes, since these elements are used to drive the lattice. Model discrepancy with experiments for a modulated magnetic lattice with sinusoidal modulation is discussed in more detail in Ref. [24,34].

## IV. WAVENUMBER BANDGAP BREATHERS

We start the discussion of wavenumber bandgap breathers by considering the idealized situation of no damping ($c = 0$). If all wavenumbers are outside of the gap, then every plane wave will be linearly stable (i.e., all Floquet multipliers will lie on the unit circle). Now consider two Floquet multipliers moving along the unit circle as an underlying system parameter is varied until they coalesce at $-1$. At this critical parameter value, the modes associated with the $-1$ multiplier will have underlying temporal period $2T$, signaling a period-doubling bifurcation. Varying the system parameter further, the two multipliers that coalesced at $-1$ will split along the real axis, with one exceeding unity in modulus. In the top right of Fig. 5, an example Floquet spectrum is shown where such a bifurcation has occurred. The black multiplier represents the unstable mode, with corresponding Floquet exponent $\mu = \sigma + i\pi/T$ (in the dispersion diagram, this mode would

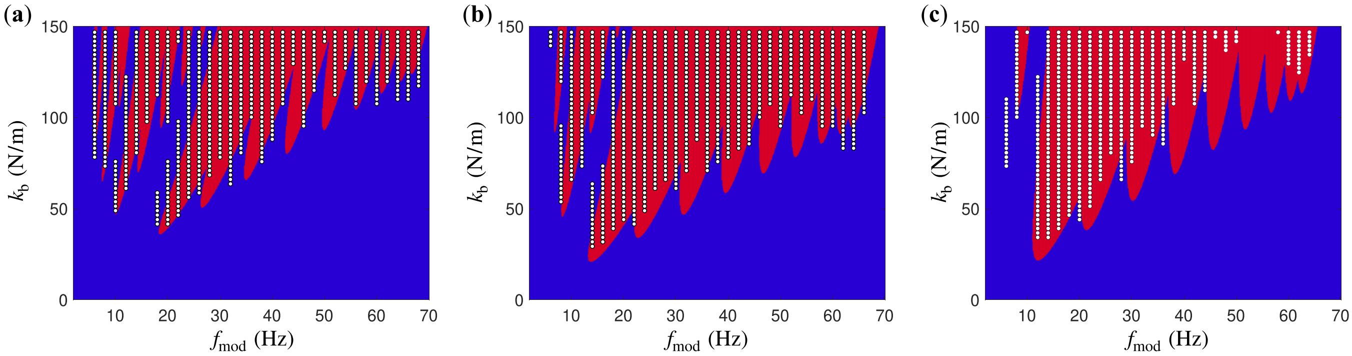

FIG. 4. Stability diagram in the ($f_{\mathrm{mod}}, k_b$) plane for $c = 0.15$ N s/m and (a) $\tau = 0.3$, (b) $\tau = 0.5$, and (c) $\tau = 0.7$. Red indicates instability and blue indicates stability. The white markers superimposed on these panels are the parameter values where the experiment was observed to be unstable. A solution is considered unstable in the experimental setup if an initially at rest lattice that is impacted on one boundary does not come to rest. If it does come to rest, it is called stable.

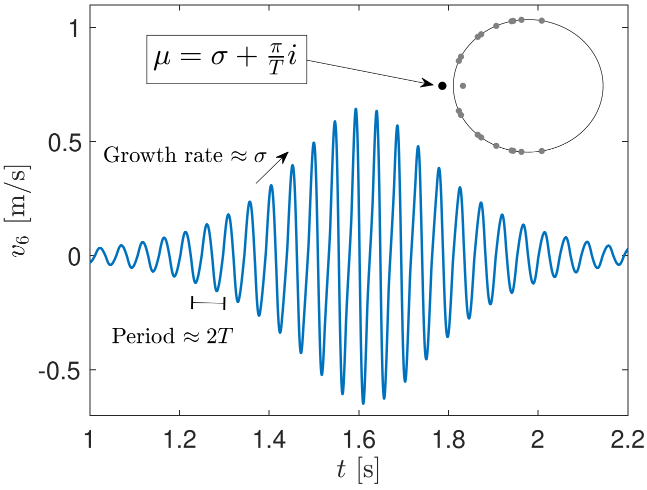

FIG. 5. Velocity profile of the sixth node $[\dot{u}_6(t) = v_6(t)]$ upon initialization of Eq. (1) with an unstable plane wave, $u_n(0) = 10^{-4}\sin(q_5 n)$. The parameter values are $k_b = 50$ N/m, $\tau = 0.5$, $T = 1/42$ s ($f_{\mathrm{mod}} = 42$ Hz), and $c = 0$ N s/m. For these parameter values, the wavenumber $q_5$ falls into a $q$-gap, with associated Floquet exponent $\mu \approx 5.764 + 42\pi i$. The underlying oscillation has an approximate period of $2T$. The excitation initially grows exponentially with rate $\sigma \approx 5.764$, but reaches a turning point, and then decays exponentially with the same rate. This is the so-called wavenumber bandgap breather. The Floquet spectrum is shown in the top right of the figure. The larger black multiplier lying outside the unit circle corresponds to wavenumber $q_5$.

lie in the wavenumber bandgap). In the example of Fig. 5, the relevant unstable mode corresponds to $q_5$. If one were to initialize the linear model with this unstable mode, namely, $u_n(0) = \sin(q_5 n)$, the solution would oscillate with period $2T$ and would grow exponentially with rate $\sigma$. If one takes the same type of initial data, namely, $u_n(0) = a\sin(q_5 n)$ where $0 < a \ll 1$, for the nonlinear equations of motion, then it is possible that a wavenumber bandgap ($q$-gap) breather is generated. This is precisely what is shown in Fig. 5. Evidently, the nonlinearity of the system enabled the temporal localization of the structure. The remainder of the paper will be dedicated to understanding the nature of the $q$-gap breather.

The $q$-gap breather shown in Fig. 5 is a natural first example, since it has exactly one wavenumber in the $q$-gap. For larger values of the modulation amplitude, $k_b$, the gap size will increase, and thus more wavenumbers will tend to fall into the gap. For the experimental realization of $q$-gap breathers we required larger modulation amplitudes (discussed in Sec. IV D). Thus, for our next example, we select $k_b = 150$ N/m and $f_{\mathrm{mod}} = 45$ Hz, see Fig. 6. The wavenumbers $q_5 = 5\pi/11$ and $q_4 = 4\pi/11$ fall into the gap $(q_\ell, q_r) \approx (0.93, 1.52)$. The $q_5$ wavenumber is quite close to right band edge. In particular the distance to the edge is $\Delta q = q_r - q_5 \approx 0.09$. The Floquet exponent associated with this wavenumber is $\mu_5 = \sigma_5 + i\omega_5 = 4.8107 + i45\pi$. Like the first example, we initialize the dynamics with $u_n(0) = a\sin(q_5 n)$. The excitation grows, and then decays, exponentially with rate given by $\sigma_5$. This happens uniformly within the lattice, as shown by the intensity plot in Fig. 6(a). Figure 6(b) shows the time series of the velocity of the sixth node (solid blue curve). Both Figs. 6(a) and 6(b) demonstrate that the dynamics are localized in time. Spatial periodicity of the solution is imposed by construction due to the finite length of the lattice with zero boundary conditions. The role of space and time have been switched when compared with the classic breathers of space-periodic systems, and the underlying wavenumber lies in a $q$-gap. Thus, the solution shown in Fig. 6 is another example of $q$-gap breather. Note that the $q$-gap breather was able to form despite the existence of another wavenumber in the gap, namely, $q_4$. The role of additional modes in the gap is discussed in Sec. IV D.

The breather envelope of a space-periodic FPUT lattice is described by a soliton of the NLS equation (in the limit of the temporal frequency approaching the band edge from within the spectral gap). Motivated by this fact, we fit the velocity profile $v_6$ with a function of the form $\beta_1 \mathrm{sech}\,[\sigma_5(t - \beta_2)]$ where $\beta_j$ are fitting parameters and $\sigma_5$ is the real part of the Floquet exponent. See the gray dashed line of Fig. 6(b). The good agreement between the velocity profile and the fit

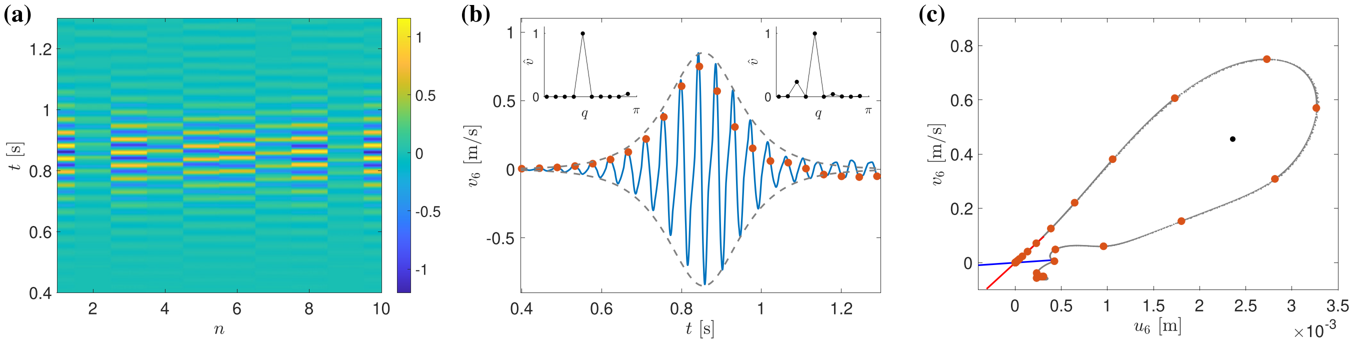

FIG. 6. Wavenumber bandgap breather for $k_b = 150$ N/m, $\tau = 0.5$, $f_{\mathrm{mod}} = 45$ Hz and $c = 0$ N s/m in various representations. (a) Intensity plot of velocity after initializing the dynamics with an unstable mode with wavenumber $q_5$. The temporal localization is uniform throughout the lattice. (b) Time series of the velocity of node 6 of panel (a). The dashed line shows the best-fit envelope. The red dots are the solution sampled every $2T$ seconds. The insets show the spatial Fourier transform before (left) and after (right) the turning point. (c) Plot of the Poincaré map in the $(u_6, v_6)$ plane (red dots). In particular, a plot of the solution shown in (b) sampled every $2T$ seconds is shown [note the red dots of panel (c) correspond to the red dots in panel (b)]. The gray line is the near homoclinic orbit that is generated by initializing the Poincaré map with several different initial values along the unstable eigenvector of the zero state. The unstable (stable) eigenvectors are shown as red (blue) lines near the origin. The near homoclinic orbit surrounds a $2T$ periodic solution (black marker).

envelope function indicates that the growth and decay rates are indeed given by the real part of the associated Floquet exponent, in this case $\sigma_5$.

### A. Dynamical systems view of *q*-gap breathers

To better understand the mechanism behind the formation of the wavenumber bandgap breather, we construct a Poincaré map of the dynamics by sampling the solution with the period associated with the breather, namely, $2T$. Thus, the map will be of the form $\mathbf{F}_j(\mathbf{u}^0) = \mathbf{u}(2Tj)$, where $j$ is an integer, and $\mathbf{u} = (u_1, u_2, \dots, u_{N-1}, v_1, v_2, \dots, v_{N-1}) \in \mathbb{R}^{2(N-1)}$ is vector valued solution of Eq. (1) with initial value $\mathbf{u}^0$. As in the simulation shown in Fig. 6(b), the initial value of the map is given by an unstable mode (e.g., with wavenumber $q_5$). The red dots of Fig. 6(b) show values of the map $\mathbf{F}$ that correspond to $v_6$ and Fig. 6(c) show values of $\mathbf{F}$ in the $(u_6, v_6)$ phase plane. The eigenvector corresponding to the unstable (stable) Floquet exponent $\mu_5$ $(-\mu_5)$ is shown in red (blue). The gray line of Fig. 6(c) is obtained by repeatedly generating the map $\mathbf{F}$ in the $(u_6, v_6)$ plane for various (small) multiples of the initial value $\mathbf{u}^0$. The origin is a saddle type fixed point, and the trajectory forms a near homoclinic orbit that surrounds a time-periodic solution with period $2T$ [the black dot of Fig. 6(c)]. The periodic orbit was obtained by applying Newton's method to the equation $0 = \mathbf{F}(\mathbf{u}^0) - \mathbf{u}^0$. The dynamical systems view of the waveform allows us to see the interplay of the stability of the zero state (with exact stability analysis performed in Sec. III) and the nonlinearity of the system leading naturally to a near homoclinic orbit. The orbit is not exactly homoclinic, since it does not approach the origin via the stable eigenvector as $t \to \infty$. Indeed, as can also be inferred from Fig. 6(b), the solution does not decay to zero, but rather it experiences small oscillations. This is due to the existence of other modes in the system (e.g., ones with associated multipliers lying on the unit circle), which are excited during the dynamic evolution. The insets of Fig. 6(b) show a normalized spatial Fourier transform of the signal before (the left inset) and after (the right inset) the maximum velocity is attained. In particular, the quantity $|\hat{v}|/|\max \hat{v}|$ is shown against the wavenumber, where $\hat{v}(q) = \frac{2}{N-1}\sum_n v_n(t)\sin(nq)$ where $t = 0.66$s and $t = 1.02$s are the times used to compute the transform before and after the turning point, respectively. Before the turning point the only prominent wavenumber is the one associated with the initial value (in this case $q_5 = 5\pi/11$). After the turning point, there is an additional mode excited that lies outside the wavenumber bandgap (in this case $q_3 = 3\pi/11$). It is this mode that is primarily responsible for the nonzero oscillations at the tail of the breather. If one imposes the additional criterion that a breather must have tails decaying to zero, then strictly speaking, the structure found here would be a generalized breather, since the orbit is not exactly homoclinic. Classic breathers with tails that do not decay to zero are common in continuous nonintegrable systems, and have sometimes been referred to as generalized breathers [45]. Over longer time windows, the amplitude of the signal can grow again (leading to a repeated appearance of breathers), but eventually the structure typically breaks down, leading to chaotic type dynamics for long-time simulations, see Fig. 7. Similar observations have been made for k-gap solitons in photonic systems [35], where the soliton pattern repeats until it eventually breaks down.

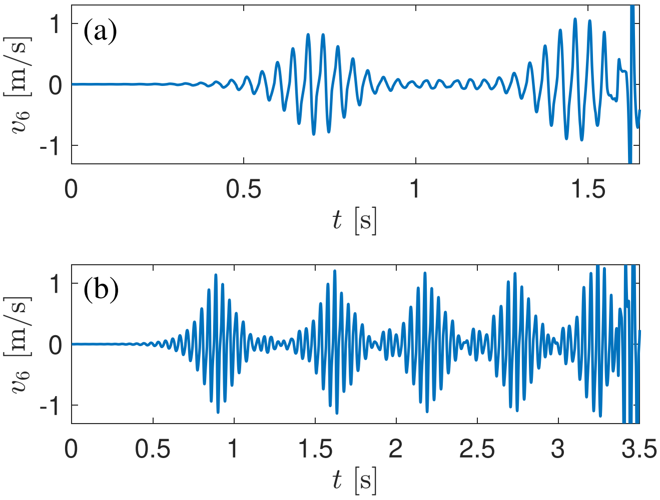

FIG. 7. (a) Same simulation as Fig. 6(b) but over a longer time interval. The breathing pattern appears twice before breaking down, and exhibits possible chaotic dynamics. (b) Same as panel (a), but with $k_b = 90$ N/m. The breathing pattern repeats several times, but it also eventually breaks down.

### B. Families of *q*-gap breathers

$q$-gap breathers for other values of the duty cycle, $\tau$, and lattice length are qualitatively similar to those of Fig. 6. Some examples are provided in Appendix B. In this section, we focus rather on generating a family of wavenumber bandgap breathers parametrized by the distance the underlying wavenumber is from the band edge. For the breather shown in Fig. 6 the distance to the edge is $\Delta q = q_r - q_5 \approx 0.09$. This is a natural parameter to consider, as the distance to the band edge determines breather width and amplitude in space-periodic systems [1]. Keeping all parameters fixed, but gradually varying the modulation frequency $f_{\text{mod}}$ has the effect of shifting the bandgap in the wavenumber axis. Thus, we fix the wavenumber ($q_5$ in this case), whose distance to the right edge will increase as the modulation frequency is increased. In particular, we have that $\Delta q = q_r(f_{\text{mod}}) - q_5$. To find the value of $q_r$ in the model, we find values of $q$ such that $G_D = -1$, where $G_D$ is defined in Eq. (8). The larger of the two solutions of $G_D = -1$ will be $q_r$. Note that it is possible for a bandgap to open when $G_D = 1$, but that is not the case for the parameter set chosen for the present study. It is also possible in principle that multiple bandgaps can exist, but this situation is not considered here. By construction, $\Delta q = 0$ will be precisely when the mode $q_5$ is at the band edge. In terms of the linear theory, $\Delta q = 0$ corresponds to two Floquet multipliers coalescing at $-1$ on the unit circle. There is some critical modulation frequency at which this occurs, which we call $f_{\text{mod}}^{\text{model}}$.

For each value of $f_{\text{mod}}$ (and hence $\Delta q$) we generate a $q$-gap breather using the procedure described in the previous section, namely, we initialize the dynamics with the mode $a\sin(q_5 n)$. The amplitude of the resulting breather is computed as the maximum velocity of the sixth node, i.e., $\max_t \|v_6(t)\|$. The

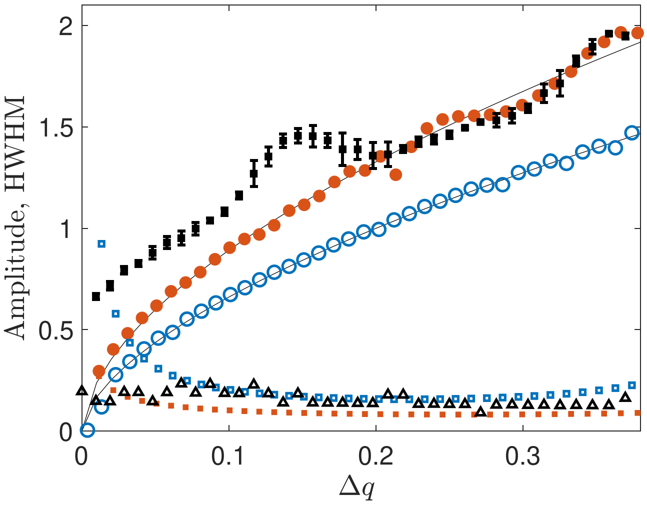

FIG. 8. Plot of the breather amplitude for the $c = 0$ N s/m (red dots) and $c = 0.15$ N s/m (blue circles) simulations vs distance of the wavenumber to the band edge, $\Delta q$. The other parameter values are $k_b = 150$ N/m and $\tau = 0.5$. The lines show the best-fit function of the form $\beta_1 \Delta q^{\beta_2}$. The markers with error bars are the measured amplitude from the experiment. The solid red squares and open blue squares show the theoretical HWHM for the $c = 0$ N s/m and $c = 0.15$ N s/m cases, respectively. The black triangles are the experimentally measured HWHM.

red dots of Fig. 8 show the amplitude of the breather vs $\Delta q$. Note that the breather becomes larger in amplitude as the wavenumber goes deeper into the $q$-gap, namely, as $\Delta q$ increases.

The amplitude data is fit with a function of the form $\beta_1 \Delta q^{\beta_2}$, with the best-fit values being $\beta_1 = 3.34$ and $\beta_2 = 0.57$ (see the solid line in Fig. 8 passing through the red dots). This is consistent with the trend found for discrete breathers in space-periodic systems where it is well known that the breather amplitude grows like $O(\sqrt{\Delta\omega})$, where $\Delta\omega$ is the difference between the breather frequency and the edge of the frequency spectrum [1]. Moreover, discrete breathers typically bifurcate from one (not both) of the band edges. Which edge is determined by the nonlinearity of the system (leading to a so-called hardening inequality [1]). Simulations of our temporally periodic lattice with modes with wavenumber near the left edge of the bandgap ($q_5 \approx q_\ell$) did not lead to the robust formation of breathers, suggesting that an analog to the hardening inequality of discrete breathers may exist in this setting too.

### C. The role of damping on *q*-gap breathers

Now that we have established the existence of wavenumber bandgap breathers in Eq. (1), we consider the role of damping, which will bring us closer to the experimentally relevant conditions. Breathers in experiments will always be a dissipative analog of breathers in lossless models. To motivate a modified definition, we repeat the simulations shown in Fig. 6 but with a nonzero damping parameter. The yellow square (blue circle) markers of Fig. 9(a) show the orbit with a damping parameter of $c = 0.075$ ($c = 0.15$) N s/m. The orbit starts close to being homoclinic, but the dynamics are attracted to a stable fixed point (i.e., a time-periodic orbit of the original system with period $2T$). This fixed point exists in the lossless ($c = 0$) system too [shown as the black marker of Fig. 6(c)], but it is not asymptotically stable. The orbit in the damped system experiences an initial exponential growth and a turning point, like the lossless breather, but rather than approaching near zero amplitude, the dynamics tend to the stable fixed point. Thus, the left tail of the "damped breather" (in the time domain) is much like a lossless breather, whose amplitude is slightly lower due to the presence of damping. The right tail of the "damped breather" approaches a periodic oscillation, whose amplitude is not necessarily small relative to the amplitude of the breather. See Fig. 9(b) for an example time series with $c = 0.15$ N s/m. Simulations with other values of the damping constant $c$ are qualitatively similar. Examples are given in Appendix B.

As in the previous section, we also generate a family of damped $q$-gap breathers for various modulation frequencies (and hence $\Delta q$ values) for the damping value $c = 0.15$ N s. The breather amplitude is shown as the blue circle markers in Fig. 8. The qualitative amplitude trend is similar to the lossless

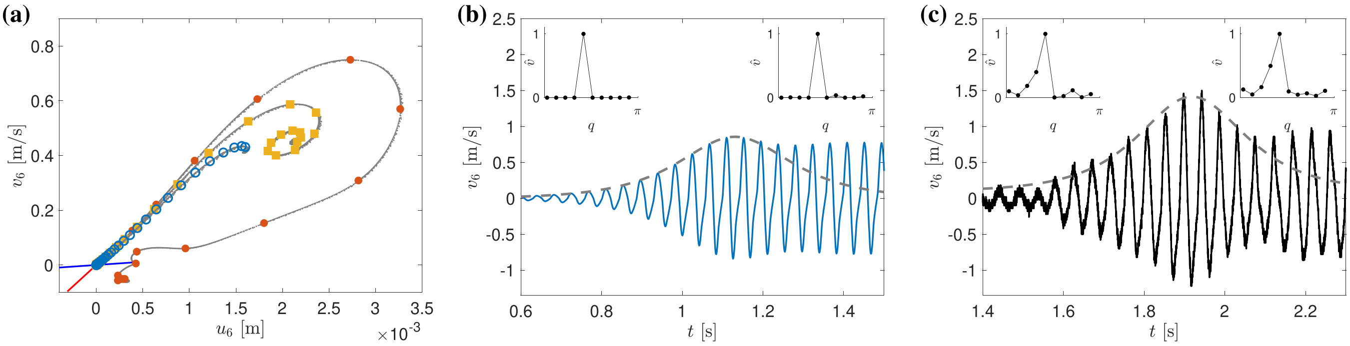

FIG. 9. (a) Poincaré maps with $c = 0.075$ N s/m (yellow squares) and $c = 0.15$ N s/m (blue circles) showing how damping affects the near homoclinic orbit [shown for reference in red markers, see also Fig. 6(c)]. The parameter values are $k_b = 150$ N/m, $\tau = 0.5$ and $f_{\text{mod}} = 45$ Hz. The gray lines are generated by initializing the Poincaré map with several different initial values along the unstable eigenvector of the zero state. (b) Time series example for the $c = 0.15$ N s/m simulation with $\Delta q = 0.147$ ($f_{\text{mod}} = 45$ Hz). The dashed line shows the best-fit envelope of the solution up until the maximum. The insets show the spatial Fourier transform before (left) and after (right) the turning point. (c) Same as panel (b), but for the experiment with $\Delta q = 0.147$ ($f_{\text{mod}} = 45.2$ Hz).

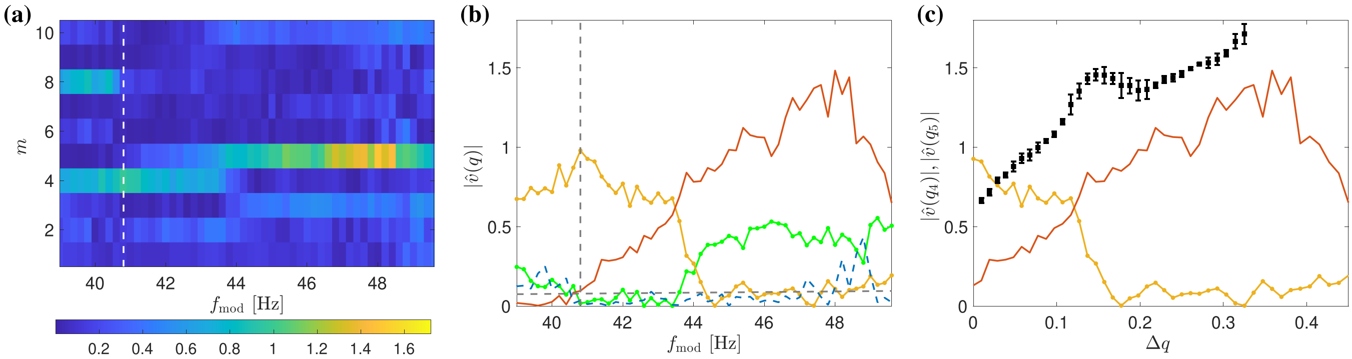

FIG. 10. (a) Intensity plot of Fourier amplitude in the ($f_{\rm mod}$, $m$) plane, where $m$ is the mode number. The Fourier transform was applied to the experimental data after the $q_5$ mode was excited using the procedure detailed in the text. Color intensity corresponds to the absolute value of the spatial Fourier transform of the velocity at the peak of the time series. The parameter values are $k_b = 150$ N/m and $\tau = 0.5$. The vertical dashed line is the modulation frequency where the $m = 5$ mode changes stability. (b) Plot of the absolute value of the Fourier modes $m = 3$ (green dotted line), $m = 4$ (yellow dotted line), $m = 5$ (red line) and $m = 6$ (blue dashed line) vs modulation frequency $f_{\rm mod}$. The horizontal dashed line is the Fourier amplitude cutoff value used to determine when mode $m = 5$ changes stability (the red line). The vertical dashed line is the corresponding modulation frequency. (c) Same as panel (b), but only the $m = 4$ (yellow dotted line) and $m = 5$ (red line) modes are shown. The horizontal axis is now $\Delta q$. By construction $\Delta q = 0$ corresponds to the vertical dashed line of panel (a). The markers with error bars are maximum velocity of the sixth node (taken from Fig. 8). The small spike in amplitude can partially be explained by the emergence of the $q_4$ mode.

case, but the amplitude is decreased. The amplitude data in the damped case is also fit with a function of the form $\beta_1 \Delta q^{\beta_2}$, with the best-fit values being $\beta_1 = 2.62$ and $\beta_2 = 0.59$, see the solid line passing through the blue circles in Fig. 8.

### D. Experimental realization of *q*-gap breathers

We now turn to the experimental construction of wavenumber bandgap breathers using the dissipative definition of a breather defined above. To initialize the experiment with a mode with wavenumber $q_m$, the unmodulated system is driven with the frequency $\omega_{\rm disp}(q_m)$. This will excite a waveform with wavenumber and frequency concentration at $q_m$ and $\omega_{\rm disp}(q_m)$, respectively, and is thereby approximate to a linear traveling plane wave. Once the desired plane wave is excited, the initial driving is turned off, and the modulation is turned on simultaneously. The waveform in the experimental chain at the time the modulation is turned on will be approximate to the initial condition used in the simulations of the modulated chain at $t = 0$. Like in the damped simulation, the amplitude in the experiment will initially grow, reach a turning point, decay, but eventually approach a periodic orbit (or exhibit chaotic behavior). An example experimental time series is shown in Fig. 9(c). Notice the qualitative agreement to the theoretical prediction shown in Fig. 9(b).

To generate a family of $q$-gap breathers, a method to estimate the distance to the band edge in the experiment, $\Delta q$, must first be established. Recall from Sec. IV B that $\Delta q = 0$ corresponds to a change in stability of the mode $q_5$, which occurs for some critical modulation frequency $f_{\rm mod}^{\rm model}$. In general, the critical modulation frequency in the experiment will be different, which we call $f_{\rm mod}^{\rm expt}$. To determine when a particular mode (e.g., $q_5$) changes stability in the experiment, we inspect the spatial Fourier transform. We call the Fourier amplitude of a particular mode the absolute value of the spatial Fourier transform of the velocity at the peak of the time series. The Fourier amplitudes are shown in Fig. 10(a,b) after the mode $q_5$ is excited. It can be seen that the procedure to excite the $q_5$ mode does indeed create a waveform that has wavenumber concentration near $q_5$ (in particular, see the $f_{\rm mod} > 45$ Hz range). Imperfections in the experimental procedure, however, will inevitability excite other modes (the consequence of these additional modes is discussed below). At some critical modulation frequency (what we are calling $f_{\rm mod}^{\rm expt}$), the $q_5$ mode will become stable, and this in turn will result in a very small Fourier amplitude of the $q_5$ mode. We define the cutoff amplitude based on the measured amplitude of the noise of the system, see the horizontal dashed line of Fig. 10(b). The cutoff modulation frequency corresponding to this amplitude is approximately 40.8 Hz. This frequency now represents the experimental value of the critical modulation frequency, $f_{\rm mod}^{\rm expt}$. To have $\Delta q = q_r - q_5 = 0$ in the experiment when $q_r$ is evaluated with the critical modulation frequency $f_{\rm mod}^{\rm expt}$, we define $\Delta q = q_r(f_{\rm mod} - \delta f_{\rm mod}) - q_5$, where $\delta f_{\rm mod} = f_{\rm mod}^{\rm expt} - f_{\rm mod}^{\rm model}$. In this way, $\Delta q = 0$ corresponds to the frequency at which $q_5$ becomes unstable for both experiment and model.

With a method to estimate $\Delta q$ in the experiment now in place, we can plot the amplitude of the breather as a function of $\Delta q$, see the error bars in Fig. 8. The qualitative amplitude trend agrees with the theoretical prediction. The breather amplitude in the experiment increases as $\Delta q$ increases, just as in the theoretical prediction, but the amplitude is underestimated by the theory (compare the error bars to the blue markers). The underestimation can also be seen in the time series example shown in Figs. 9(b) and 9(c). This can be partially explained by the fact that other modes (including unstable ones) in the experiment besides $q_5$ are excited. In Fig. 10(b), it can be seen that the Fourier amplitude of the $q_4$ mode (yellow dotted line) is non-negligible, even though the waveform shown was the result of exciting the $q_5$ mode. The insets of Fig. 9(c) show the spatial Fourier transform of the experiment before ($t = 1.6$ s) and after ($t = 2.2$ s) the turning point, with both demonstrating non-negligible amplitude of the unstable $q_4$ mode. This is in contrast with the theoretical simulation, where $q_4$ is also unstable, yet is not excited in the theoretical evolution, see insets of Fig. 9(b). This is due to the fact that we can initialize the model simulation with an exact $q_5$ mode, which can only be done approximately in the experiment.

The effect of additional modes on the breather amplitude is also evident in Fig. 10(c). The markers with error bars from Fig. 8, showing the experimental breather amplitude, have been superimposed on Fig. 10(c). Notice that the small spike in amplitude of the black error bars coincides with the emergence of the $q_4$ mode (yellow dotted line). Thus, breathers for modulation frequencies with a non-negligible unstable $q_4$ mode are also experiencing growth in that mode, which will lead to amplitudes that will be larger than the predictions. This partly explains why the amplitude trend of the theory in Fig. 8 underestimates the experimental observation. Note that the parameter values used in this study were determined before any stability or breather experiments were conducted (using the procedure detailed in Ref. [34]). While additional parameter tuning may lead to better quantitative agreement, we find overall that the qualitative behavior is captured quite well with the untuned model.

In all the examples considered thus far, the presence of modes in addition to $q_5$ affected the observed dynamics. It is worth summarizing and comparing these effects. In the lossless case ($c = 0$), these modes are not initially present but are instead excited as the waveform experiences growth due to the instability of the $q_5$ mode. It is the coupling to such modes that causes small oscillations in the right tail of the structure and is ultimately responsible for the breakdown of the structure. In all simulations we preformed, the additional excited modes laid outside of the $q$-gap and were therefore neutrally stable. In the damped case ($c \neq 0$), additional stable modes may also be excited during the dynamic evolution, but the dynamics are eventually attracted to a stable-periodic orbit, and hence, there is no observation of chaotic dynamics. On the contrary, in the experiments, other modes are excited initially, namely, in the process of exciting the $q_5$ mode. In particular, unstable modes (such as $q_4$) are also initially present. It is the presence of additional *unstable* modes that leads to larger amplitudes.

Finally, we measure the width of the structures using the half-width at half maximum (HWHM) metric. The HWHM is given by $t_{\text{max}} - t_{\text{half}}$, where $t_{\text{max}}$ is the time the maximum is attained and $t_{\text{half}}$ is the time where the trajectory first attains half the maximum value. We use the half width (as opposed to full width) in the metric since the right tail of the structure is affected by the presence of damping, see Figs. 9(b) and 9(c). Using the half width allows for better comparison of the structure for various values of the damping constant. The experimentally measured values are shown as the black triangles in Fig. 8. The width of the structure can be predicted theoretically using the real part of the Floquet exponent. In particular, assuming the envelope of the breather follows the form $a\,\text{sech}(\sigma t)$, which we demonstrated previously was a reasonable assumption, we can compute the HWHM as $\text{sech}^{-1}(1/2)/\sigma_5$. The prediction in the lossless ($c = 0$) and damped ($c = 0.15$ N s/m) cases are shown as red solid squares and open blue squares, respectively, in Fig. 8. For sufficiently large values of $\Delta q$, there is good agreement between theory and experiment, and both show the structure becomes more narrow as the wavenumber goes deeper into the gap. This is consistent with discrete breathers in space periodic systems [1].

### E. Contrasting *q*-gap breathers and discrete breathers

The $q$-gap breathers studied here share a number of properties with classical discrete breathers. This includes the envelope function being well described by a hyperbolic secant, the breather amplitude being proportional to the square-root of the wavenumber's (or frequency in case of discrete breathers) distance to the gap edge, and the fact that breathers typically bifurcate from one edge of the gap (exceptions include stiffness-dimers [46] and mass-in-mass chains [47] where breathers can bifurcate from both edges). There are, however, key differences. At the linear level in spatially periodic, temporally homogeneous lattices, all plane waves are stable. It is only in the presence of nonlinearity that plane waves can exhibit instability. In comparison, plane waves can be unstable in linear temporally periodic, spatially homogeneous lattices. In terms of breather formation this has practical implications. For systems with a frequency gap, a breather can form by initializing the dynamics with a plane wave at the edge of the linear spectrum. The amplitude of the plane wave ultimately determines the temporal frequency of the resulting classical breather [1]. For systems with a $q$-gap, any plane wave with wavenumber in the $q$-gap can be used for initialization, and the underlying frequency and wavenumber of the resulting breather are approximately equal to the corresponding linear frequency and wavenumber. Discrete breathers are discrete in the axis of localization and so coupling to higher-order harmonics can be avoided due to the band limited nature of the spectrum [1]. This implies that discrete breathers can be long-lived. The $q$-gap breathers studied here are continuous in the axis of localization, and hence, coupling with other modes is unavoidable in general, leading to small oscillating tails and eventual break down of the structure. For classical breathers in continuous systems, coupling to other modes also occurs in generic systems [45]. The exceptions are integrable equations, in which case coupling to other modes vanishes due to the underlying integrable structure [48]. For nonintegrable, spatially continuous systems, the Hamiltonian structure can be exploited to bound the amplitude of the tails [45]. The system studied here is not integrable and there is no Hamiltonian structure, so it is not clear if the system can be constructed in such a way to avoid growth of the tails. However, since the system is finite and discrete in space, it would be possible in principle to construct a system where all wavenumbers fall into some gap. In this case, genuine homoclinic orbits could be possible. The existence of such solutions is a further direction this study motivates.

## V. CONCLUSION

We provided the first experimental evidence of wavenumber bandgap ($q$-gap) breathers, and corroborated results with analysis and direct numerical simulations. $q$-gap breathers are structures that are localized in time, periodic in space, and have wavenumber in a $q$-gap. They are the direct analog of the discrete breathers of spatially periodic lattices, which are of fundamental importance in a diverse range of fields.

We studied $q$-gap breathers in the context of a time-varying phononic lattice. The key ingredient for the formation of such solutions was the opening of a $q$-gap. For a stiffness given by a time-periodic step function, we computed an exact condition for the opening of a $q$-gap and verified the stability predictions against experiments directly. We showed that the $q$-gap breathers become narrower and larger in amplitude as the underlying wavenumber moves deeper into the $q$-gap, both in experiment and theory. The dynamical systems view of the solutions with no damping showed that the orbits in the phase plane were not exactly homoclinic but rather experienced small oscillations due to the presence of neutrally stable modes. The coupling to such modes causes the eventual breakdown of the structure over long time simulations. In the presence of damping, the solutions approached a time-periodic orbit, but the transition to this state was still well described by the undamped breather solution.

There are several avenues of inquiry that follow naturally from this study, including establishing rigorously the existence of $q$-gap breathers with oscillating tails, the possible existence of genuine $q$-gap breathers (i.e., with both tails decaying to zero), the numerically exact computation of $q$-gap breathers (i.e., numerical roots of the appropriate map up to a user-prescribed tolerance) and an analytical description of the breather profiles via a multiple-scales analysis. The exploration of such structures in higher spatial dimensions or in other settings beyond the phononic or photonic realm would also be of great interest. $q$-gap breathers seem to be generic and may be possible in a wide class of nonlinear time-varying systems with a $q$-gap. Recent advances in experimental platforms for other time-varying phononic as well as photonic and electric systems suggest that $q$-gap breathers could be relevant there as well. $q$-gap breathers offer an alternative mechanism for controllable temporal localization, which may have applications in the creation of frequency combs, energy harvesting applications, or signal processing. Moreover, any system that is already described by a nonlinear wave equation that could be adapted to be time-varying (in order to induce a $q$-gap) would be a candidate for the implementation of $q$-gap breathers. This suggests that $q$-gap breathers' relevance could extend beyond physics to fields such as chemistry, biology, and more.

## ACKNOWLEDGMENTS

This material is based upon work supported by the U.S. National Science Foundation under Grant No. DMS-2107945 (C.C. and E.W.) and the Science and Technology Center New Frontiers of Sound (NewFoS) Grant No. 2242925. The authors are grateful for discussions with P. G. Kevrekidis.

## APPENDIX A: MODULATION INSTABILITY CALCULATIONS

In this Appendix, we are considering the linearized dynamics,

$$M\ddot{u}_n = K(u_{n-1} - 2u_n + u_{n+1}) - k(t)u_n - c\dot{u}_n, \tag{A1}$$

where $K = \alpha A d^{\alpha-1}$. We now derive an exact condition for stability in this equation, discussing first the case of no damping ($c = 0$) before moving on to the damped lattice case.

### 1. Undamped case

Making the ansatz $u_n(t) = X_m(n)\Theta_m(t)$, one finds upon substitution into Eq. (A1) that the spatial and temporal parts satisfy, respectively,

$$\lambda_m X_m(n) = -X_m(n-1) + 2X_m(n) - X_m(n+1), \tag{A2}$$

$$\ddot{\Theta}_m = \frac{-\lambda_m K - k(t)}{M}\Theta_m. \tag{A3}$$

The eigenvalue problem Eq. (A2) subject to the Dirichlet boundary conditions $X(0) = X(N) = 0$ has the eigenvalues $\lambda_m = 4\sin^2(q_m/2)$ where the wavenumber is $q_m = m\pi/N$ with $m = 1, \dots, N-1$. The associated eigenfunctions are $X_m(n) = \sin(q_m n)$. Equation (A3) has the form of a Hill's equation when $k(t)$ is assumed to be periodic [49]. In the case that the modulation coefficient is given by a step-function we can obtain an exact solution and stability condition. To motivate the approach to achieve this, consider that the general solution of the Hill's equation will be a superposition of functions of the form

$$\Theta_m(t) = H_m(t)e^{i\omega_m t}, \tag{A4}$$

where $H_m(t)$ is a function with the same period as $k(t)$ and $\pm i\omega_m$ is a Floquet exponent [49]. Due to the symmetries of Eq. (A3) (which has no damping), $\omega_m$ will either be real, in which case the underlying solution will be stable, or $\omega_m$ will be purely imaginary, in which case the underlying solution will be unstable. The general solution of Eq. (A1) will thus be unstable, since it is simply a superposition of the $N-1$ solutions of the form $X_m(n)\Theta_m(t)$.

We now find an expression that will indicate if $\omega_m$ is real, or purely imaginary, which will be our stability condition. We suppose that $H_m(t)$ is a piecewise function with period $T$,

$$H_m(t) = \begin{cases} H_{a,m}(t), & 0 \leqslant t < \tau T \\ H_{b,m}(t), & \tau T \leqslant t < T, \end{cases} \quad H_m(t+T) = H_m(t). \tag{A5}$$

Upon substitution of Eq. (A4) into Eq. (A3) we obtain for $0 \leqslant t < \tau T$,

$$\ddot{H}_{a,m}(t) = \left(\omega_m^2 - \frac{\lambda_m K + k_a}{M}\right)H_{a,m}(t) - 2i\omega_m\dot{H}_{a,m}(t), \tag{A6}$$

and for $\tau T \leqslant t < T$ we have

$$\ddot{H}_{b,m}(t) = \left(\omega_m^2 - \frac{\lambda_m K + k_b}{M}\right)H_{b,m}(t) - 2i\omega_m\dot{H}_{b,m}(t). \tag{A7}$$

Equations (A6) and (A7) have the general solutions, respectively,

$$H_{a,m}(t) = e^{-i\omega_m t}[A\cos(s_{a,m}t) + B\sin(s_{a,m}t)], \tag{A8}$$

$$H_{b,m}(t) = e^{-i\omega_m t}[C\cos(s_{b,m}t) + D\sin(s_{b,m}t)], \tag{A9}$$

where $A, B, C, D$ are arbitrary constants and

$$s_{a,m} = \sqrt{\frac{\lambda_m K + k_a}{M}}, \quad s_{b,m} = \sqrt{\frac{\lambda_m K + k_b}{M}}.$$

Demanding that $H_m(t)$ is continuous and differentiable at $t = 0$ and $t = \tau T$ leads to the following four conditions:

$$\begin{aligned}
0 &= e^{-i\omega_m \tau T} \cos{(s_{a,m}\tau T)} A + e^{-i\omega_m \tau T} \sin{(s_{a,m}\tau T)} B \\
&\quad - e^{-i\omega_m \tau T} \cos{(s_{b,m}\tau T)} C - e^{-i\omega_m \tau T} \sin{(s_{b,m}\tau T)} D, \\
0 &= A - e^{-i\omega_m T} C \cos{(s_{b,m}T)} - e^{-i\omega_m T} D \sin{(s_{b,m}T)}, \\
0 &= -e^{-i\omega_m \tau T}[s_{a,m} \sin{(s_{a,m}\tau T)} + i\omega_m \cos{(s_{a,m}\tau T)}]A \\
&\quad + e^{-i\omega_m \tau T}[s_{a,m} \cos{(s_{a,m}\tau T)} - i\omega_m \sin{(s_{a,m}\tau T)}]B \\
&\quad + e^{-i\omega_m \tau T}[s_{b,m} \sin{(s_{b,m}\tau T)} + i\omega_m \cos{(s_{b,m}\tau T)}]C \\
&\quad - e^{-i\omega_m \tau T}[s_{b,m} \cos{(s_{b,m}\tau T)} - i\omega_m \sin{(s_{b,m}\tau T)}]D, \\
0 &= -i\omega_m A + B s_{a,m} + C e^{-i\omega_m T}[s_{b,m} \sin{(s_{b,m}T)} \\
&\quad + i\omega_m \cos{(s_{b,m}T)}] - D e^{\omega_m T}[s_{b,m} \cos{(s_{b,m}T)} \\
&\quad - i\omega_m \sin{(s_{b,m}T)}].
\end{aligned}$$

The above system of homogeneous linear equations for $(A, B, C, D)$ has nontrivial solutions only if its determinant vanishes. This condition leads to the following equation for $\omega_m$,

$$\begin{aligned}
\cos{(\omega_m T)} &= \cos{(s_{a,m}\tau T)} \cos{[s_{b,m}(1-\tau)T]} \\
&\quad - \frac{s_{a,m}^2 + s_{b,m}^2}{2 s_{a,m} s_{b,m}} \sin{(s_{a,m}\tau T)} \sin{[s_{b,m}(1-\tau)T]} \\
&\equiv G_0. \qquad \text{(A10)}
\end{aligned}$$

Since the magnitude of the left-hand side of this equation cannot exceed unity for real $\omega$, we have a condition for instability. In particular $|G_0| > 1$ implies that $\omega$ must be imaginary and thus the underlying solution is unstable. This result is similar to those obtained in photonic systems [43].

### 2. Damped case

In the presence of damping ($c \neq 0$), the temporal part of the separated solution $\Theta_m(t)$ satisfies

$$\ddot{\Theta}_m = \frac{-\lambda_m K - k(t)}{M} \Theta_m - \frac{c}{M} \dot{\Theta}_m, \qquad \text{(A11)}$$

where the eigenvalues $\lambda_m$ remain unchanged. In the presence of the damping term, we cannot assume that the existence of a Floquet exponent with real part implies instability. Thus, a slightly more general form of the solution is assumed

$$\Theta_m(t) = H_m(t) e^{\mu_m t}, \qquad \text{(A12)}$$

where $\mu_m = \sigma_m + i\omega_m$ is the Floquet exponent where $\sigma_m, \omega_m \in \mathbb{R}$. Note, this is in contrast with the previous section where $\omega_m$ was allowed to be imaginary, which made the analysis slightly simpler. Here, we have dedicated terms for the real and imaginary part of the Floquet exponent, with $\sigma_m > 0$ implying instability. Following the process described in the previous section with the modified ansatz given by (A12), we find the following determinant equation:

$$\begin{aligned}
&\exp\left[-\left(\sigma_m + \frac{c}{2M}\right)T\right][\cos{(\omega_m T)} - i \sin{(\omega_m T)}] \\
&\quad + \exp\left[\left(\sigma_m + \frac{c}{2M}\right)T\right][\cos{(\omega_m T)} + i \sin{(\omega_m T)}] = 2G,
\end{aligned} \qquad \text{(A13)}$$

where $G$ has the same definition as $G_0$ in Eq. (A10), but with

$$\begin{aligned}
s_{a,m} &= \frac{1}{2}\sqrt{\frac{4(\lambda_m K + k_a)}{M} - \left(\frac{c}{M}\right)^2}, \\
s_{b,m} &= \frac{1}{2}\sqrt{\frac{4(\lambda_m K + k_b)}{M} - \left(\frac{c}{M}\right)^2}.
\end{aligned}$$

Note that if $c = 0$ and $\sigma_m = 0$ then $G_0 = G$ and Eq. (A13) is identical to Eq. (A10). Separating Eq. (A13) into real and imaginary parts we obtain

$$G = \cosh\left[\left(\sigma_m + \frac{c}{2M}\right)T\right] \cos{(\omega_m T)}, \qquad \text{(A14)}$$

$$0 = \sinh\left[\left(\sigma_m + \frac{c}{2M}\right)T\right] \sin{(\omega_m T)}. \qquad \text{(A15)}$$

These are Eqs. (6) and (7) of the main text. Since $\sigma_m \leqslant 0$ implies stability, these equations imply the following stability condition:

$$|G_D| \leqslant 1, \quad G_D \equiv G \operatorname{sech}\left(\frac{cT}{2M}\right), \qquad \text{(A16)}$$

which is Eq. (8) of the main text.

## APPENDIX B: MORE EXAMPLES OF *q*-GAP BREATHERS

In the main text we primarily considered the parameter set $k_b = 150$ N/m, $\tau = 0.5$ s, and $c = 0$ or $c = 0.15$ N s/m. In this Appendix we provide a few examples of $q$-gap breather for other parameter sets.

We start with a lattice of size $N = 301$, $k_b = 150$ N/m, $\tau = 0.5$, $c = 0$ N s/m, and $f_{\text{mod}} = 52$ Hz. For a lattice this large, there will be a large number of wavenumbers that fall into the gap. Figure 11 shows an example of such a simulation that was initialized with an unstable mode with $q = 181\pi/301$. In Fig. 11(a), the time series of the velocity of the node $n = 150$ is shown. The pulse is localized in time. The insets show the spatial Fourier transform before ($t = 0.48$ s) and after the turning point ($t = 1.86$ s). During the dynamic evolution, the (stable) mode $q = 240\pi/301$ is excited. The excitation of such modes ultimately leads to the eventual break down of the structure, as seen in Fig. 11(a) and also in the main text for examples in lattices with length parameter $N = 11$ (see Fig. 7).

We excite $q$-gap breathers for several wavenumbers in the bandgap [for these parameter values the gap is (1.35,1.9)]. In particular, for each wavenumber $q_m$ considered, we simulate the dynamics with initial condition given by the mode $10^{-4} \sin(q_m n)$. The amplitude is taken to be the maximum velocity in the considered time domain, $\max_{0<n<N} \max_t v_n(t)$. Note, this is in contrast with the amplitude metric in the main text, which only measures the amplitude of the sixth node. Since the wavenumber is changing, the amplitude of an individual node will also change upon changing the wavenumber. Thus, a smoother metric in this case is to take the max velocity

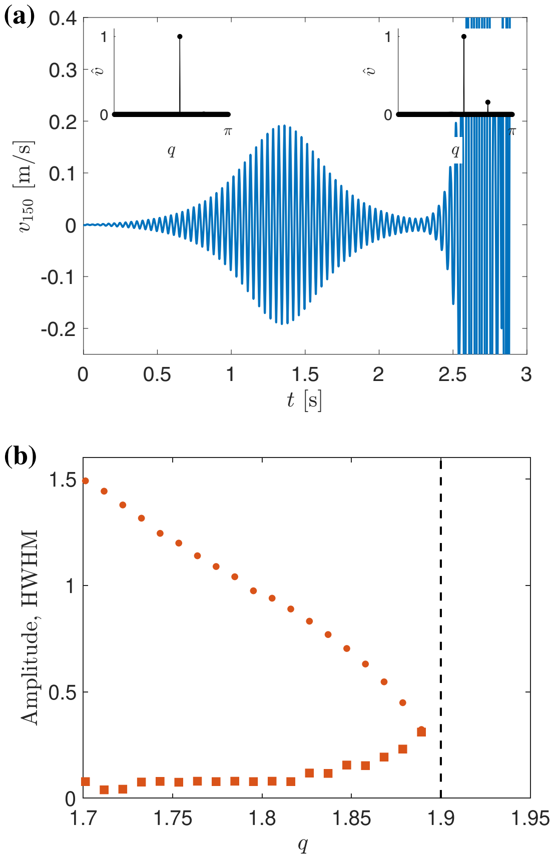

FIG. 11. (a) Wavenumber bandgap breather for $\tau = 0.5$, $k_b = 150$ N/m, $f_{\text{mod}} = 52$ Hz, $c = 0$ N s/m, and $N = 301$. Velocity profile of the $n = 150$ node is shown. While the structure is temporally localized, it eventually breaks down. (b) Plot of the amplitude (red dots) and half width at half maximum (HWMH) (red squares) of breathers bifurcating from the right band edge of the wavenumber bandgap. The vertical black dashed line is the edge of the bandgap.

among all nodes. The width of the solution is measured to be half the width at half the maximum of the solution (HWHM), as in the main text. As Fig. 11(b) shows, the wavenumber gap breather follows the same trend as shown in the main text; the amplitude increases and the width decreases as the wavenumber goes deeper into the gap. At some point, the breather no longer forms ($q \approx 1.7$).

We now return to the lattice size of the experiment, with $N = 11$. In this case, the wavenumber bandgap breathers are qualitatively similar for other values of the duty cycle $\tau$, as seen in Fig. 12.

Figure 13 shows how the wavenumber bandgap breather evolution is affected by the presence of damping. A value of the modulation amplitude $k_b$ that is different from the main text is used ($k_b = 90$ N/m in this example). For nonzero damping, there exists a nonzero fixed point that can be asymptotically stable that the dynamics are eventually attracted to. In the transient regime, as the damping is increased, the time between consecutive peaks in the re-occurrence decreases (compare the $c = 0.01$ N s/m and $c = 0.05$ N s/m panels). For larger values of the damping constant the stable fixed point (i.e., a time periodic orbit with period $2T$) is approached fairly quickly (see the $c = 0.15$ N s/m panel).

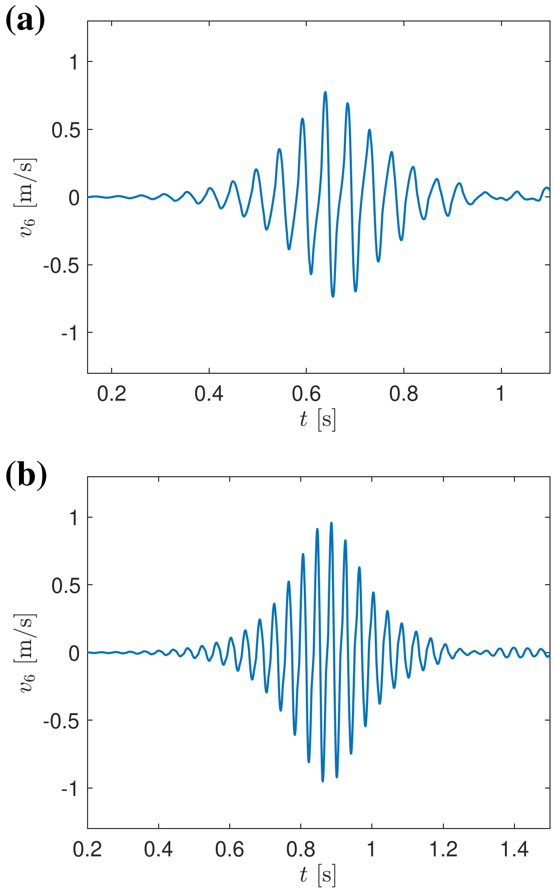

FIG. 12. Wavenumber bandgap breathers for $k_b = 150$ N/m, $c = 0$, $N = 11$ and various $\tau$ values. Velocity of the sixth node is shown. (a) Breather with $\tau = 0.3$ and $f_{\text{mod}} = 49.4$ Hz. (b) Breather with $\tau = 0.7$ and $f_{\text{mod}} = 42.34$ Hz.

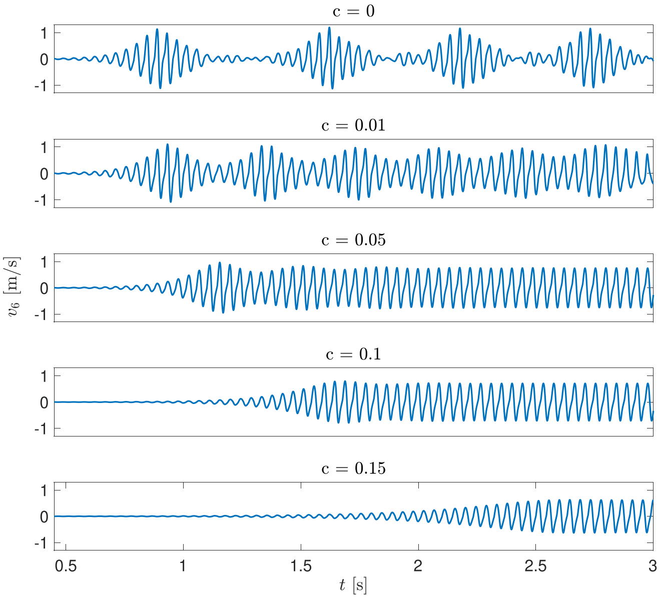

FIG. 13. Examples of wavenumber bandgap breathers for $k_b = 90$ N/m, $f_{\text{mod}} = 45$ Hz, $\tau = 0.5$, and $N = 11$ and various $c$ N s/m values.

[1] S. Flach and A. Gorbach, Discrete breathers: Advances in theory and applications, Phys. Rep. **467**, 1 (2008).

[2] M. A. Butt, S. N. Khonina, and N. L. Kazanskiy, Recent advances in photonic crystal optical devices: A review, Opt. Laser Technol. **142**, 107265 (2021).

[3] M. A. Porter, P. G. Kevrekidis, and C. Daraio, Granular crystals: Nonlinear dynamics meets materials engineering, Phys. Today **68**(11), 44 (2015).

[4] M. Peyrard, Nonlinear dynamics and statistical physics of DNA, Nonlinearity **17**, R1 (2004).

[5] D. K. Campbell, S. Flach, and Yu. S. Kivshar, Localizing energy through nonlinearity and discreteness, Phys. Today **57**(1), 43 (2004).

[6] P. G. Kevrekidis, Non-linear waves in lattices: Past, present, future, IMA J. Appl. Math. **76**, 389 (2011).

[7] S. V. Dmitriev, E. A. Korznikova, Yu. A. Baimova, and M. G. Velarde, Discrete breathers in crystals, Phys. Usp. **59**, 446 (2016).

[8] S. Flach, M. V. Ivanchenko, and O. I. Kanakov, $q$-breathers and the Fermi-Pasta-Ulam problem, Phys. Rev. Lett. **95**, 064102 (2005).

[9] L. Liu, W.-R. Sun, B. A. Malomed, and P. G. Kevrekidis, Time-localized dark modes generated by zero-wave-number-gain modulational instability, Phys. Rev. A **108**, 033504 (2023).

[10] L. S. Cao, D. X. Qi, R. W. Peng, Mu Wang, and P. Schmelcher, Phononic frequency combs through nonlinear resonances, Phys. Rev. Lett. **112**, 075505 (2014).

[11] M. Yu, J. K. Jang, Y. Okawachi, A. G. Griffith, K. Luke, S. A. Miller, X. Ji, M. Lipson, and A. L. Gaeta, Breather soliton dynamics in microresonators, Nat. Commun. **8**, 14569 (2017).

[12] N. Akhmediev, A. Ankiewicz, and J. M. Soto-Crespo, Rogue waves and rational solutions of the nonlinear Schrödinger equation, Phys. Rev. E **80**, 026601 (2009).

[13] A. Ankiewicz, N. Akhmediev, and J. M. Soto-Crespo, Discrete rogue waves of the Ablowitz-Ladik and Hirota equations, Phys. Rev. E **82**, 026602 (2010).

[14] A. Chowdury, W. Chang, and M. Battiato, From rogue wave solution to solitons, Phys. Rev. E **107**, 014212 (2023).

[15] M. Soljačć, M. Ibanescu, S. G. Johnson, Y. Fink, and J. D. Joannopoulos, Optimal bistable switching in nonlinear photonic crystals, Phys. Rev. E **66**, 055601(R) (2002).

[16] F. Y. Wang, G. X. Li, H. L. Tam, K. W. Cheah, and S. N. Zhu, Optical bistability and multistability in one-dimensional periodic metal-dielectric photonic crystal, Appl. Phys. Lett. **92**, 211109 (2008).

[17] C.-P. Wen, W. Liu, and J.-W. Wu, Tunable terahertz optical bistability and multistability in photonic metamaterial multilayers containing nonlinear dielectric slab and graphene sheet, Appl. Phys. A: Mater. Sci. Process. **126**, 426 (2020).

[18] S. Mukherjee and M. C. Rechtsman, Observation of unidirectional solitonlike edge states in nonlinear Floquet topological insulators, Phys. Rev. X **11**, 041057 (2021).

[19] D. A. Powell, I. V. Shadrivov, and Y. S. Kivshar, Multistability in nonlinear left-handed transmission lines, Appl. Phys. Lett. **92**, 264104 (2008).

[20] A. B. Kozyrev, H. Kim, and D. W. van der Weide, Parametric amplification in left-handed transmission line media, Appl. Phys. Lett. **88**, 264101 (2006).

[21] D. A. Powell, I. V. Shadrivov, and Y. S. Kivshar, Asymmetric parametric amplification in nonlinear left-handed transmission lines, Appl. Phys. Lett. **94**, 084105 (2009).

[22] M. Moghaddaszadeh, M. A. Attarzadeh, A. Aref, and M. Nouh, Complex spatiotemporal modulations and non-Hermitian degeneracies in $\mathcal{PT}$-symmetric phononic materials, Phys. Rev. Appl. **18**, 044013 (2022).

[23] J. R. Reyes-Ayona and P. Halevi, Observation of genuine wave vector ($k$ or $\beta$) gap in a dynamic transmission line and temporal photonic crystals, Appl. Phys. Lett. **107**, 074101 (2015).

[24] Y. Wang, B. Yousefzadeh, H. Chen, H. Nassar, G. Huang, and C. Daraio, Observation of nonreciprocal wave propagation in a dynamic phononic lattice, Phys. Rev. Lett. **121**, 194301 (2018).

[25] E. Galiffi, P. A. Huidobro, and J. B. Pendry, Broadband nonreciprocal amplification in luminal metamaterials, Phys. Rev. Lett. **123**, 206101 (2019).

[26] G. Trainiti, Y. Xia, J. Marconi, G. Cazzulani, A. Erturk, and M. Ruzzene, Time-periodic stiffness modulation in elastic metamaterials for selective wave filtering: Theory and experiment, Phys. Rev. Lett. **122**, 124301 (2019).

[27] S. Lee, J. Park, H. Cho, Y. Wang, B. Kim, C. Daraio, and B. Min, Parametric oscillation of electromagnetic waves in momentum band gaps of a spatiotemporal crystal, Photonics Res. **9**, 142 (2021).

[28] G. Trainiti and M. Ruzzene, Non-reciprocal elastic wave propagation in spatiotemporal periodic structures, New J. Phys. **18**, 083047 (2016).

[29] B. M. Goldsberry, S. P. Wallen, and M. R. Haberman, Non-reciprocal wave propagation in mechanically-modulated continuous elastic metamaterials, J. Acoust. Soc. Am. **146**, 782 (2019).

[30] Y. Chen, X. Li, H. Nassar, A. N. Norris, C. Daraio, and G. Huang, Nonreciprocal wave propagation in a continuum-based metamaterial with space-time modulated resonators, Phys. Rev. Appl. **11**, 064052 (2019).

[31] X. Zhu, J. Li, C. Shen, X. Peng, A. Song, L. Li, and S. A. Cummer, Non-reciprocal acoustic transmission via space-time modulated membranes, Appl. Phys. Lett. **116**, 034101 (2020).

[32] J. Marconi, E. Riva, M. Di Ronco, G. Cazzulani, F. Braghin, and M. Ruzzene, Experimental observation of nonreciprocal band gaps in a space-time-modulated beam using a shunted piezoelectric array, Phys. Rev. Appl. **13**, 031001(R) (2020).

[33] H. Nassar, B. Yousefzadeh, R. Fleury, M. Ruzzene, A. Alù, C. Daraio, A. N. Norris, G. Huang, and M. R. Haberman, Nonreciprocity in acoustic and elastic materials, Nat. Rev. Mater. **5**, 667 (2020).

[34] B. L. Kim, C. Chong, S. Hajarolasvadi, Y. Wang, and C. Daraio, Dynamics of time-modulated, nonlinear phononic lattices, Phys. Rev. E **107**, 034211 (2023).

[35] Y. Pan, M.-I. Cohen, and M. Segev, Superluminal $k$-gap solitons in nonlinear photonic time crystals, Phys. Rev. Lett. **130**, 233801 (2023).

[36] A. Ganesan, C. Do, and A. Seshia, Phononic frequency comb via intrinsic three-wave mixing, Phys. Rev. Lett. **118**, 033903 (2017).

[37] G. Lee, D. Lee, J. Park, Y. Jang, M. Kim, and J. Rho, Piezoelectric energy harvesting using mechanical metamaterials and phononic crystals, Commun. Phys. **5**, 94 (2022).

[38] M. Safaei, H. A. Sodano, and S. R. Anton, A review of energy harvesting using piezoelectric materials: State-of-the-art

a decade later (2008-2018), Smart Mater. Struct. **28**, 113001 (2019).

[39] W. Hartmann, *Acoustic Signal Processing* (Springer, New York, 2007), pp. 503–530.

[40] E. Fermi, J. Pasta, S. Ulam, and M. Tsingou, Studies of nonlinear problems, Tech. Rep. Los Alamos Scientific Laboratory Report No. LA-1940, 1955 [reprinted in Lect. Appl. Math. **15**, 143 (1974)].

[41] H. Nassar, X. C. Xu, A. N. Norris, and G. L. Huang, Modulated phononic crystals: non-reciprocal wave propagation and Willis materials, J. Mech. Phys. Solids **101**, 10 (2017).

[42] I. Kovacic, R. Rand, and S. M. Sah, Mathieu's equation and its generalizations: overview of stability charts and their features, Appl. Mech. Rev. **70**, 020802 (2018).

[43] M. Centurion, M. A. Porter, Y. Pu, P. G. Kevrekidis, D. J. Frantzeskakis, and D. Psaltis, Modulational instability in nonlinearity-managed optical media, Phys. Rev. A **75**, 063804 (2007).

[44] Z. Rapti, G. Theocharis, P. G. Kevrekidis, D. J. Frantzeskakis, and B. A. Malomed, Modulational instability in Bose-Einstein condensates under Feshbach resonance management, Phys. Scr. **2004**, 27 (2004).

[45] M. D. Groves and G. Schneider, Modulating pulse solutions for quasilinear wave equations, J. Differ. Equations **219**, 221 (2005).

[46] M. M. Lee, E. G. Charalampidis, S. Xing, C. Chong, and P. G. Kevrekidis, Breathers in lattices with alternating strain-hardening and strain-softening interactions, Phys. Rev. E **107**, 054208 (2023).

[47] J. A. D. Wattis, Breather modes of fully nonlinear mass-in-mass chains, Phys. Rev. E **105**, 054212 (2022).

[48] J. Cuevas, P. G. Kevrekidis, and F. L. Williams, *The Sine-Gordon Model and its Applications: From Pendula and Josephson Junctions to Gravity and High Energy Physics* (Springer-Verlag, Heidelberg, 2014).

[49] A. H. Nayfeh and D. T. Mook, *Nonlinear Oscillations* (Wiley and Sons, Weihheim, 2004).